J Nanopart Res (2011) 13:5615–5626
DOI 10.1007/s11051-011-0249-7

SPECIAL ISSUE: NANOSTRUCTURED MATERIALS 2010

Evidence for magnetic interactions among magnetite nanoparticles dispersed in photoreticulated PEGDA-600 matrix

P. Allia · P. Tiberto · M. Coisson · A. Chiolerio · F. Celegato · F. Vinai · M. Sangermano · L. Suber · G. Marchegiani

Received: 7 September 2010 / Accepted: 18 January 2011 / Published online: 5 February 2011

Abstract Magnetite nanoparticles having mean diameter of about 8 nm have been prepared by a thermo-chemical route. Different amounts (5 and 10% wt) of a stable dispersion of magnetite nanoparticles in *n*-hexane were added to polyethylene glycol diacrylate (PEGDA-600) oligomer containing 2% wt of radicalic photoinitiator. The homogenized mixture was poured on a silica glass substrate and the resulting film was photoreticulated in N_2 atmosphere using a UV lamp. As a result, a polymer-based magnetic nanocomposite was obtained, where the magnetic nanoparticles are dispersed in the diamagnetic matrix, as checked by SEM. Morphology, composition, and size of as-prepared nanoparticles were checked by SEM and X-ray diffraction. The magnetic properties of magnetite nanoparticles prior to and after inclusion in the polymeric matrix have been studied by means of an alternating-gradient magnetometer (T interval: 10–300 K, H_{MAX}: 18 kOe). FC-ZFC curves were obtained in the same temperature interval. The results show that the nanocomposites cannot be simply described as containing superparamagnetic particles undergoing an anisotropy-driven blocking and that collective magnetic interactions play a non-negligible role. Low-temperature hysteretic properties indicate that the polymeric matrix affects the effective anisotropy of magnetite nanoparticles. Dispersion of magnetite NPs in PEGDA has non-trivial consequences on their magnetic properties.

Keywords Magnetite nanoparticles · PEGDA · Interacting superparamagnets · Colloids

P. Allia (✉) · A. Chiolerio · M. Sangermano · G. Marchegiani
Politecnico di Torino DISMIC, Corso Duca degli Abruzzi 24, 10125 Torino, TO, Italy
e-mail: paolo.allia@polito.it

P. Tiberto · M. Coisson · F. Celegato · F. Vinai
INRIM, Electromagnetism, Strada delle Cacce 91, 10135 Torino, TO, Italy

L. Suber · G. Marchegiani
ISM-CNR, Area della Ricerca di Roma 1, Via Salaria km 29.500, Monterotondo Scalo, 00016 Roma, RM, Italy

Introduction

In the past decade, the development of nanotechnology allowed for the fabrication and tailoring of the functional properties of hybrid materials composed of inorganic nanoparticles (NPs) dispersed within polymer matrices and potentially exploited for a number of applications, either in micro-/nanoelectronics or biomedicine (Nicolais and Carotenuto 2005). These novel materials are being actively investigated because of the new properties originating from the combination of inorganic components and polymers. The polymeric matrix is inherently processable and flexible, while inorganic nanosized particles typically

exhibit unique properties that differ from those of their bulk counterparts due to the combined action of nanoscale size and strain effects, NP–matrix interface phenomena, and nanostructure morphology (Shull et al. 1994; Sohn et al. 1998).

Nanocomposite polymeric materials containing either metallic or insulating NPs have been prepared to obtain interesting physical [optical (Li et al. 2010)], conductive (Chiolerio et al. 2010; Gangopadhyay and De 2000), and magnetic (Shull et al. 1994; Sohn et al. 1998) properties for use in micro-/nanoelectronics (sensors, electrical–magnetic shields and electrochemical displays (Vázquez et al. 2004; Jalali and Wuthrich 2009), and in data storage (high-capacity magnetic storage media) (Dai et al. 2010).

Magnetic ferrofluids containing magnetite NPs surrounded by a polymer shell are being actively studied for biomedical applications (Pankhurst et al. 2003; Kumagai et al. 2009). In addition, they can be exploited as media for sprayable nanoelectronics [nanoscale integrated circuits (Jaworek and Sobczyk 2008)], and as magnetic inks in data storage (e.g., magnetic tags for smart packaging of goods) (Lee et al. 2010). In this case, the sprayable ferrofluid is an oligomer resin containing a dispersion of magnetic NPs which later is made to polymerize by heating or UV curing to form a solid film. In a number of applications, magnetic NPs are made of magnetite, a mixed-valence iron oxide with ferrimagnetic behavior. Magnetite is a cheap material with a lower degree of toxicity than metallic ferromagnets for in vivo biomedical applications. In addition, magnetite nanoparticles can be easily synthesized through a variety of low-cost techniques.

In this study, magnetite nanoparticles having mean diameter of about 8 nm have been synthesized through a thermo-chemical route and dispersed in polyethylene glycol diacrylate (PEGDA-600) oligomer subsequently submitted to UV curing. NP morphology, structure, and composition have been studied. Magnetic properties of as-received NPs and of two polymeric films containing different amounts of dispersed NPs have been measured as functions of temperature from 10 to 300 K. The role of magnetic interactions among NPs, and the interplay between NPs and the polymeric matrix have been investigated by analyzing the temperature behavior of the coercive field and the properties of field-cooled—zero-field-cooled (FC-ZFC) low-field magnetization curves.

Experimental

NP preparation

Fe_3O_4 nanoparticles (NPs) were prepared according to the method proposed by Sun et al. (Sun et al. 2004). Fe(III) acetylacetonate,1,2-hexadecanediol, oleic acid, oleylamine, benzyl ether, and *n*-hexane were purchased from Aldrich and used as received. In a typical procedure, Fe(acac)3 (2 mmol), 1,2-hexadecanediol (10 mmol), oleic acid (6 mmol), oleylamine (6 mmol), and benzyl ether (20 mL) were mixed and mechanically stirred under a flow of nitrogen. The mixture was heated under a nitrogen blanket to 200°C for 2 h and then heated up to reflux (300°C) for 1 h. The black-colored mixture was cooled to room temperature by removing the heat source and treated with ethanol under air. A dark-brown material precipitated from the solution. The product was dissolved in *n*-hexane in the presence of oleic acid and oleylamine and re-precipitated with ethanol. Finally the product was dispersed in *n*-hexane.

NP in PEGDA

The magnetite NPs dispersion in *n*-hexane was added to the PEGDA acrylic resin in two amounts, i.e., 5 and 10 phr (acronym stands for Per Hundred Resin, indicating the weight percentage amount of a fluid added to a given amount of liquid resin). The mixtures were stirred reaching a uniform dispersion and the radical photoinitiator (Irgacure 2959 Ciba) was added at a concentration of 2 wt%. The formulations were coated on glass substrates and the curing reaction was performed by irradiation with UV lamp (Hg medium pressure lamp, Italquartz, Milano, Italy) with a light intensity of about 30 mW/cm^2 (measured with EIT radiometer) for 1 min under nitrogen. UV-cured transparent films about 100 μm thick were obtained and exploited in subsequent measurements. Samples with different magnetite content will be referred to as PEGDA 5 and PEGDA 10, respectively.

Measurements

IR measurements were performed with a Perkin-Elmer FT16F PC. A few milligrams of the sample were mixed with KBr and pressed in a pellet.

X-Ray diffraction measurements were performed on a Seifert XRD 3000 P diffractometer equipped with a secondary graphite monochromator, using CuKa radiation. The measurements were in the 2θ range 20–100° with a step size of 0.02° and counting time of 2 s per step.

SEM images were obtained with a Leo 1530 FE-SEM. A few drops of sample dispersion in *n*-hexane were deposited on a graphite substrate letting the n-hexane evaporate at room temperature.

Acrylic double bond conversion was evaluated as a function of irradiation time by means of real-time FT-IR employing a Thermo-Nicolet 5700. The formulations were coated onto a silicon wafer. The sample was exposed simultaneously to the UV beam, which induces the polymerization, and to the IR beam for in situ analysis of the extent of the reaction. Acrylic double bond conversion was followed by monitoring the decrease in the absorbance, due to C=C double bonds, of the peak centered at around 1450 cm^{-1} (the acrylic double bond conversion was normalized with the carbonyl peak centered at 1700 cm^{-1}). A medium pressure mercury lamp (Hamamatsu) equipped with an optical guide was used to induce the photopolymerization (light intensity on the surface of the sample of about 30 mW/cm^2).

The gel content was determined on the cured films by measuring the weight loss after 24 h extraction with chloroform at room temperature, according to the standard test method ASTM D2765-84.

DSC measurements were performed under nitrogen flux, in the range between −20°C and 100°C, with a DSCQ 1000 of TA Instruments equipped with a low-temperature probe.

Magnetization curves were measured at fixed temperatures from 10 to 300 K on the as-received NP dried powder and on PEGDA 5 and PEGDA 10 samples by using an alternating-gradient field magnetometer (AGFM) equipped with a liquid He continuous-flux cryostat and operating in the magnetic field range -10 kOe $< H < +10$ kOe. The magnetic signal of the as-received powder is very large, while both PEGDA 5/10 samples were characterized by a very low magnetic response from embedded NPs, of the same order of magnitude of the diamagnetic contribution from sample holder, which was carefully subtracted from the measured curves. Field-cooled (FC) and zero-field-cooled (ZFC) curves were obtained by recording sample magnetization under a small constant field (H = 50 Oe) while continuously varying the measurement temperature from 10 to 250 K.

Results and discussion

The NPs were characterized by means of FT-IR spectroscopy and C, H elemental analyses to analyze the surfactant and the iron oxide phase, XRD powder diffraction to check the iron oxide phases and determine, by using the Scherrer equation, the crystallite size and SEM measurements to investigate the NP morphology and surface assembling.

The FT-IR spectrum (Fig. 1) shows the symmetric and asymmetric stretchings of the surfactant oleate—CH_2 groups at 2,920 and 2,850 cm^{-1}, the absorption of the carboxylate –CO group at 1,408 cm^{-1}, of crystallization water H_2O at 1,650 cm^{-1} and the vibration of the Fe–O bond with a sharp absorption at 585 cm^{-1} characteristic of the magnetite phase (when the oxidized phase maghemite is prevalent, the band is larger and indented). No absorption attributable to the free ligand oleic acid is detected. The C, H elemental analyses (C = 14.04, H = 2.28 w/w%, C/H atomic ratio = 0.51) are consistent with the presence of oleic acid (C/H atomic ratio = 0.55) together with one H_2O molecule in agreement with IR results. Moreover, the high value of the oleic acid percentage indicates a good surface particle capping. The X-ray powder diffraction pattern is shown in Fig. 2. The peaks are attributed to the magnetite phase; a univocal attribution by XRD is, however, not possible due to the position of the oxidized phase maghemite (γ-Fe_2O_3) peaks which are almost superimposable to the magnetite (Fe_3O_4) ones. In order to estimate the average crystallite size, D, we analyzed the peak widths at half maximum height using the Scherrer equation

$$D = (k\lambda/\beta\cos\theta) \quad (1)$$

where k is the Scherrer factor, λ is the X-ray wavelength, and β is the line broadening of a diffraction peak at 2θ angle. We found that the nanocrystals are composed by crystallites whose size is about 7.6 nm in diameter.

The particle morphology was investigated by scanning electron microscopy (SEM) (Fig. 3). The particle size is in the same range of the crystallite size

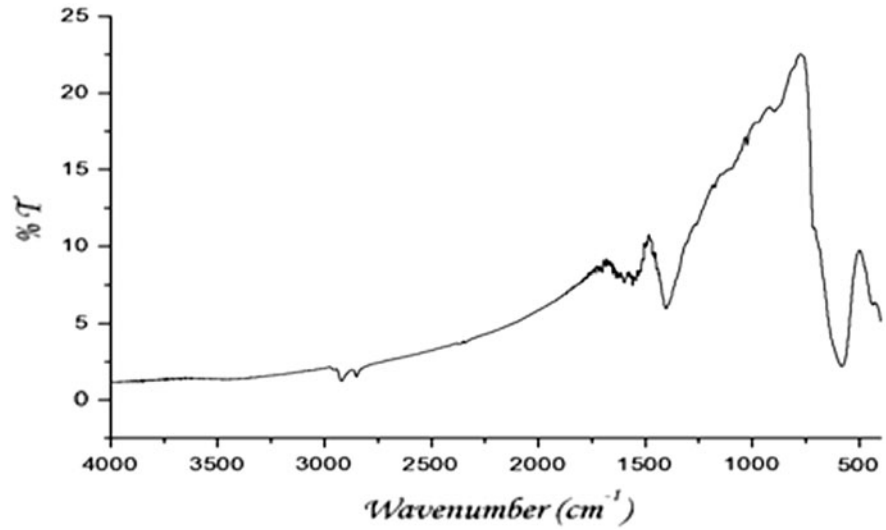

Fig. 1 FT-IR spectrum of iron oxide nanoparticles capped with oleic acid

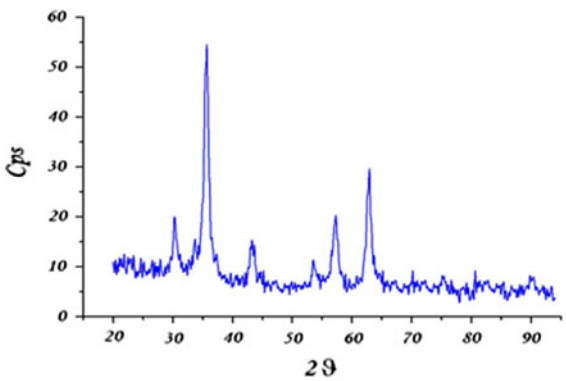

Fig. 2 XRD pattern of iron oxide nanoparticles. The peaks correspond to the magnetite/maghemite phase (see text for details)

indicating that the NPs are single crystals and their ordered assembling on the graphite substrate (see the enlargement of Fig. 3) is due to an efficient, dense capping of the surfactant to the particle surface.

The actual amount of magnetite NPs was calculated by thermo gravimetrical analysis after UV Curing and was of 0.15 and 0.3 wt%, respectively, for the formulations containing 5 and 10 phr of the added dispersion (PEGDA 5 and PEGDA 10).

The conversion curves as functions of irradiation time were practically unmodified both for the pristine PEGDA resin and for the UV-curable formulations containing an increasing amount of magnetite NPs. It can be safely assumed that the magnetic NPs do not significantly influence the rate of conversion; the acrylic double bond formation was almost complete, in all materials, after 1 min of irradiation time.

The high acrylic double bond conversion is confirmed by the high gel content values of the cured films. The gel content of the UV-cured films was always above 97%, indicating the formation of a completely insoluble network.

Differential scanning calorimetry (DSC) was performed on cured films in order to evaluate the Tg values of the cured films. It was shown that the presence of the magnetite NPs did not affect at all the mobility of the polymeric chains; the Tg values are practically the same (around −46 °C) and this is a consequence of a very low filler amount.

Representative magnetic moment curves of magnetite NPs (as-received dried powder) and PEGDA 5/10 samples are shown in Fig. 4a–c at T = 10 and 300 K in the low-mid field region. The curves taken on the two polymeric nanocomposites were previously corrected for spurious diamagnetic contributions. Note the extremely low magnetic signal measured on PEGDA 5/10 samples, which is responsible for the significant fluctuations of the magnetic signal. The magnetization of as-received NPs was calculated to be about 68 or 375 emu/cm^3 at room temperature, to be compared with 92 emu/g for bulk magnetite (Cullity 1972). The same magnetic moment per gram of *magnetic* material is presumed to be conserved for the polymeric nanocomposites also. In all cases, the curves taken at room temperature exhibit vanishingly small (nanopowder, PEGDA 5) or small

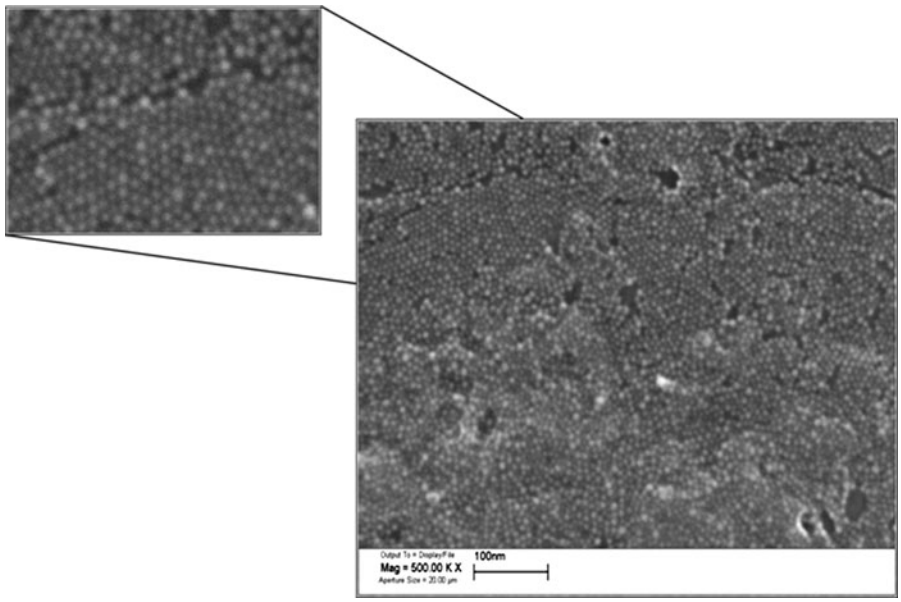

Fig. 3 Scanning electron micrograph of iron oxide nanoparticles capped with oleic acid. The enlargement shows the ordered particle assembling due to the oleic acid capping agent

(PEGDA 10) hysteresis and a typical unsaturating behavior. A magnetic hysteresis is observed at $T = 10$ K in all samples, the greatest effect being measured on the nanopowder.

In all cases, the high-temperature ($T > 40$ K), nearly anhysteretic magnetization curves are satisfactorily fitted by a single Langevin function, as indeed expected for a genuine superparamagnetic material. However, a more accurate analysis shows that the materials are not in the standard superparamagnetic regime, as evidenced by Fig. 5a where the scaling condition of reduced magnetization curves (M/M_S) when plotted as functions of H/T (as predicted for a superparamagnetic system) is shown to be not satisfied below 200 K for the nanopowder (the same r is observed in the two polymeric nanocomposites too). Instead, the reduced magnetization curves scale with the ratio H/M_S, as shown in Fig. 5b for $T = 40$ to 100 K. As known (Allia et al. 2001) this property indicates the gradual emergence of the interacting superparamagnet (ISP) regime of an NP system, where long-range interactions among isolated magnetic moments are no longer completely negligible and bring about a collective magnetic behavior which can be simply pictured by means of a mean-field approach, where the strength of the interaction is measured by a positive effective temperature T* roughly separating the ISP regime ($T < T^*$) from the standard superparamagnetic regime ($T > T^*$). A diagram showing the behavior of the ratio T*/T as a function of T is the best way to identify the various magnetic regimes of a magnetic NP system above the single-particle blocking temperature and the emergence of hysteretic phenomena (Allia et al. 2001). This plot is shown in Fig. 6 for the three studied samples. The curves are coincident within the accuracy of the ISP model, and indicate that the genuine superparamagnetic regime begins to be observed above about 100–130 K, while below this temperature all materials are in the ISP regime. The so-called collective blocking regime is never attained in the studied materials. Such a state would occur at very low temperatures, i.e., when T becomes smaller than T*/25 and is no longer sufficient to sustain the magnetic disorder, bringing about a complex freezing of magnetic moments. Of course, *single-particle* blocking effects, not accounted for by the ISP model which is connected with collective interactions only, emerge below about 40 K and act to destroy the ISP regime. The ISP model provides a more accurate estimate of the magnetic moment per particle than the usual fit to a standard Langevin function (Allia et al. 2001). It has been shown that the magnetic moment obtained by the more advanced

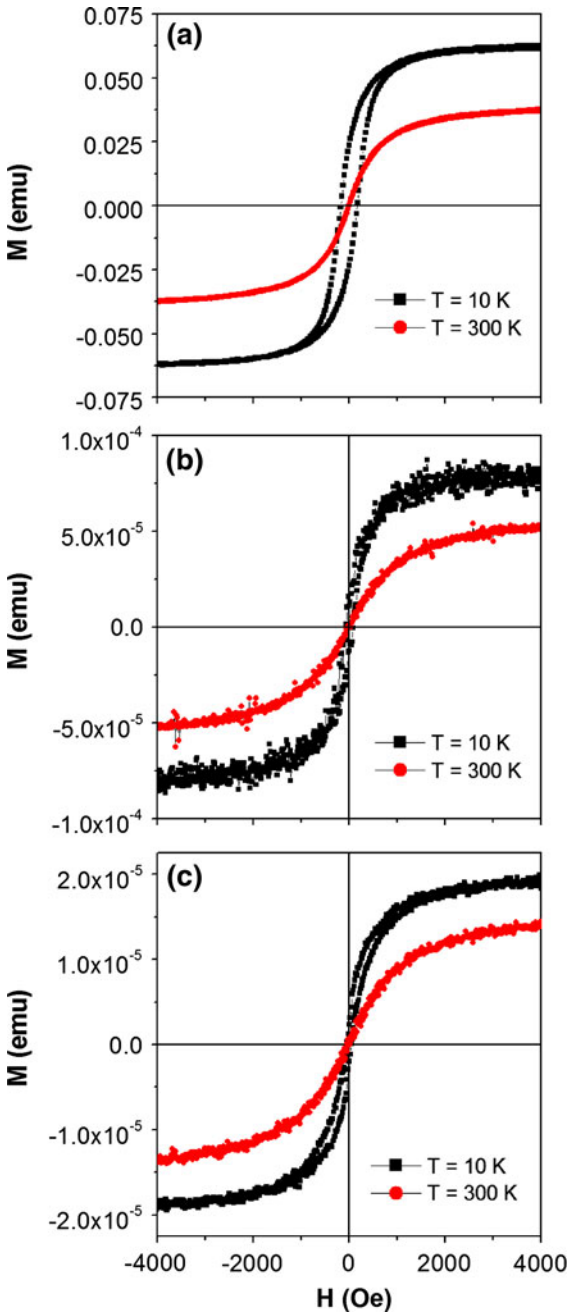

Fig. 4 Isothermal magnetization curves measured at 4 and 300 K on (**a**) NP powder; (**b**) PEGDA 5; (**c**) PEGDA 10

technique (or "true" moment) is systematically larger at each temperature than the one obtained from the simple Langevin-function fit (or "effective" moment). True and effective moments obtained from the ISP analysis are reported in Table 1 for all materials. The temperature variation of the true moment merely reflects the temperature change of the spontaneous magnetization of magnetite NPs. The effective temperature T* is also reported in Table 1. The small differences in T* among samples are not considered as significant (T* has been shown to vary between about 50 and more than 3000 K in various ISP systems). The average NP diameter obtained from the true moments using $M_S = 375$ emu/cm^3 at room temperature, as above determined, is given in the last column of Table 1. The NP diameters for PEGDA 5 and 10 are coincident (8,2 nm) and very close to the value estimated from the Scherrer analysis (7,6 nm) providing a check of the correctness of the ISP model and analysis. On the contrary, the as-received powder appears to be constituted of slightly but significantly larger NPs (9,8 nm), presumably indicating aggregation effects which are mostly inhibited when NP stable dispersions are added to PEGDA-600 oligomer.

Single-particle blocking effects are responsible for the emergence of hysteretic phenomena. The temperature behavior of the coercive field as a function of temperature is shown in Fig. 7a for all studied samples. In the case of the as-received NP powder, the coercive field becomes clearly distinguishable from experimental fluctuations below about 40 K, and steadily increases with lowering temperature up to a value of 162 Oe at 10 K. The coercive field expected for a fully blocked system of spherical magnetite NPs dominated by (volume) magnetocrystalline anisotropy is 0.64 $|K_{eff}|/M_S$ (Guardia et al. 2007). Using, as a first approximation, parameter values appropriate to bulk magnetite at 4.2 K [$M_S = 510$ emu/cm^3 and $K_{eff} = K_1 = -2 \times 10^5$ emu/cm^3 (Cullity 1972)], one would expect a coercive field of the order of 250 Oe. The value measured at 10 K is related to the presence of a fraction of NPs still in the superparamagnetic state there. Apparently, the measured coercive field rules out the presence of strong surface anisotropy effects, which should entail a much higher coercivity (Tartaj et al. 2001). The marginal role of surface anisotropy in magnetite NPs of comparable size prepared by a similar chemical route has been pointed out (Guardia et al. 2007). In PEGDA 5, the general behavior of H_C as a function of temperature is very similar to the one measured in the as-received powder. However, the low-temperature limit is significantly reduced ($H_C = 77$ Oe at 10 K). PEGDA 10 exhibits a remarkably different

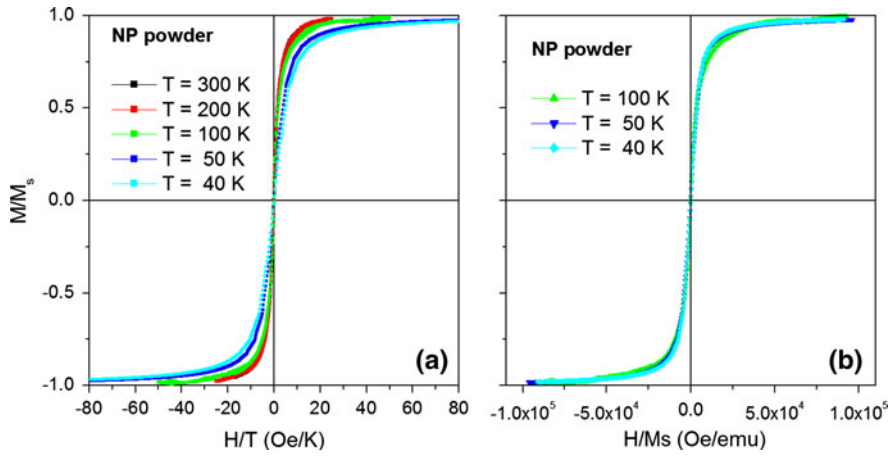

Fig. 5 Evidence of non-superparamagnetic behavior of the NP powder at intermediate temperatures: **a** the standard superparamagnetic scaling law of M/M_s as a function of H/T is not satisfied below 200 K; **b** instead, M/M_s scales as H/Ms (ISP scaling law)

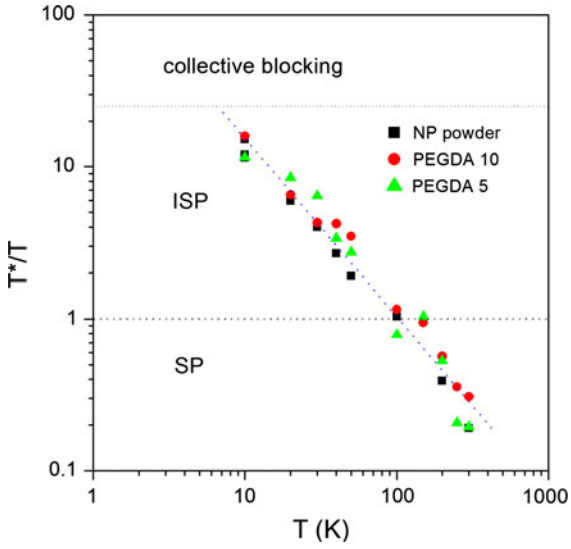

Fig. 6 ISP phase diagrams, evidencing that in all examined samples the magnetic interactions are similar. Nanoparticles act superparamagnetically well above 200 K. Collective blocking is predicted by the model to occur well below 10 K; however, this effect is completely masked by single-particle blocking (not described by the ISP model) which occurs above 10 K (see text)

behavior. A non-negligible magnetic hysteresis is present at all temperatures, and the associated coercive field ($H_C \approx 20$ Oe) is quite independent of T down to 10 K, where an enhancement up to 42 Oe is observed. This particular anomaly has no immediate explanation. It could be accounted for in terms of enhanced interactions among NPs. In the simplest approach, the appearance of a magnetic hysteresis below a given temperature is ascribed to the presence of blocked particles. However, another source of hysteresis is magnetic interaction, as previously pointed out (Allia et al. 1999). In this framework, the coercive field is a measure of the strength of dipolar interactions. In this case, the hysteretic features are almost independent of temperature and appear even at high temperatures, contrary to the case of single-particle blocking. Magnetic interactions could play a role in determining the magnetic response of PEGDA 10 possibly owing to local fluctuations of NP concentration leading to the formation of NP clusters.

Instead, NP powder and PEGDA 5 display a bona-fide single-particle blocking behavior. According to the standard Néel's model (Garcia-Otero et al. 1998), the coercive field should vary below blocking temperature according to a power law of the type $\alpha - \beta\, T^x$ (where T is the absolute temperature, and $x = 1/2$ in the case of easy magnetization axes aligned with the magnetic field direction, $x \approx 3/4$ when the easy axes are randomly distributed). In the present case, the few H_c data taken below blocking temperature do not allow for an accurate check of the validity of the power law behavior; however, they are fully compatible with a $T^{3/4}$ power law in both the NP powder and PEGDA 5, as shown in Fig. 7b. Fit to a $T^{1/2}$ law turns out to be definitely worse. In Fig. 7b, the maximum coercivity of the NP powder is predicted to reach about 260 Oe for $T \rightarrow 0$ K, in good agreement with the above reported estimate. The lower value of the coercive field in composite samples can be explained in terms of a strong reduction of the effective anisotropy constant, K_{eff} with respect to the NP powder. An independent check of this hypothesis is provided by FC-ZFC curves measured under a field of

Table 1 Magnetic and structural parameters of nanoparticles as derived from ISP analysis

Sample	Effective magnetic moment at T = 300 K (emu)[a]	True magnetic moment at T = 300 K (emu)[b]	True magnetic moment at T = 10 K (emu)[b]	T* at T = 300 K (K)[b]	Nanoparticle diameter (nm)[c]
Powder	$1{,}45 \times 10^{-16}$	$1{,}72 \times 10^{-16}$	$2{,}57 \times 10^{-16}$	110	9,8
PEGDA 5	$0{,}92 \times 10^{-16}$	$1{,}16 \times 10^{-16}$	$1{,}62 \times 10^{-16}$	120	8,2
PEGDA 10	$0{,}89 \times 10^{-16}$	$1{,}18 \times 10^{-16}$	$1{,}55 \times 10^{-16}$	130	8,2

[a] From standard Langevin-function fit in the high T limit

[b] From ISP analysis (see text for details)

[c] From magnetic analysis (using true magnetic moment value)

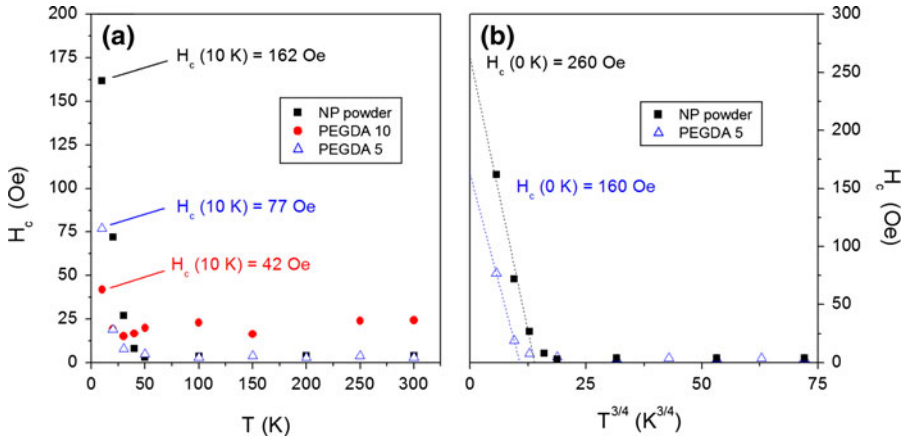

Fig. 7 (**a**) Coercive field of all examined samples as a function of temperature; (**b**) plot of coercive fields of NP powder and PEGDA 5 as functions of $T^{3/4}$

50 Oe (owing to the very low magnetic signal) and reported in Fig. 8. As known, the temperature T_M of the maximum of the ZFC curve can be used to estimate the value of K_{eff} through the relation: $T_M \approx 2 \times T_B = 2 \times |K_{eff}|V/(25\ k_B)$, T_B being the blocking temperature and V the mean NP volume (Gittleman et al. 1974). Indeed, the exact relation $T_M = 2T_B$ was derived for the idealized case of a rectangular distribution of NP volumes; however, only a slightly different expression ($T_M \approx 1.8T_B$) was obtained for the physically more significant case of a structured distribution (the Poisson's distribution). The maximum of PEGDA 5 is observed at 23 K while that of PEGDA 10 is sharper and located at 14 K. Using $V = \pi/6 \times (8.2 \times 10^{-7})^3\ cm^3 = 2.89 \times 10^{-19}\ cm^3$ in the formula for $|K_{eff}|$, this quantity is estimated to be around 1.4×10^5 emu/cm^3 in PEGDA 5 (a value slightly smaller than that of K_1 in bulk magnetite) and 8.4×10^4 emu/cm^3 in PEGDA 10. A further proof of the consistency of these measurements is given by the ratio $|K_{eff}|$(PEGDA 5)/$|K_{eff}|$(NP powder) obtained from ZFC curve maxima ($\approx 1.4 \times 10^5/2 \times 10^5$) which is close to H_c (0 K) (PEGDA 5)/H_c (0 K) (NP powder) $\approx$ 160/260 obtained from Fig. 7b, as expected.

Finally, it should be noted that the samples used for FC/ZFC measurements were different (although coming from the same preparation) from those used in isothermal magnetization measurements; as a consequence the absolute magnitude of magnetic signals reported in Figs. 4 and 8 cannot be directly compared.

Therefore, both coercive fields and ZFC curve maxima point to a reduction of $|K_{eff}|$ when magnetite NPs are embedded in the polymeric matrix. An explanation for such a puzzling behavior may be found in the interplay between crystal and stress anisotropy, the latter being induced in the NPs by the compressive stress possibly transferred by the polymeric matrix to embedded NPs. During the polymerization process, the host oligomer is subjected to shrinking; in addition, the polymeric matrix is expected to further shrink with reducing temperature at a much higher rate than the embedded NPs (Lin

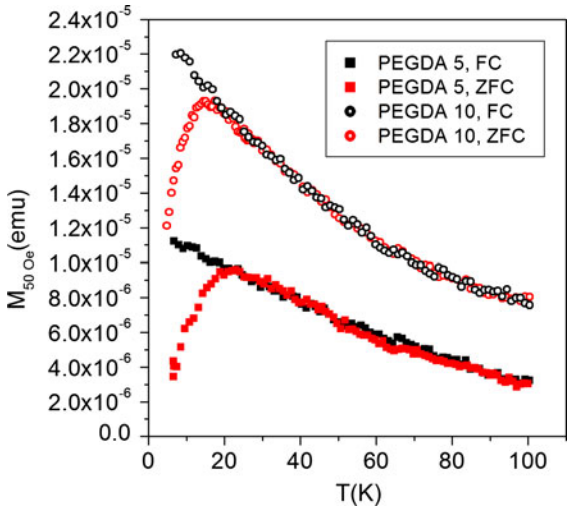

Fig. 8 FC/ZFC curves of PEGDA 5 and PEGDA 10 (applied field: 50 Oe)

and FreemanBD 2006; Nikolaev and Shipilin 2000), exerting a compressive stress on them. In the presence of a (uniaxial) stress σ, the effective anisotropy constant can be written $K_{eff} = K_1 - 3/2\ \lambda_s\ \sigma$. In magnetite, K_1 remains negative and λ_s remains positive at all temperatures (Cullity 1972; Bickford et al. 1955), so that a uniaxial compressive stress ($\sigma < 0$) of sufficiently large amplitude can act to significantly reduce K_{eff} Using the bulk value for λ_s [$\lambda_s = 40 \times 10^{-6}$, quite independent of temperature (Bickford et al. 1955)], a uniaxial compressive stress larger than 400 MPa $= 4 \times 10^9$ dyn/cm^2 would be needed to produce a stress anisotropy able to significantly reduce the $|K_{eff}|$ value.

In order to substantiate this hypothesis, we performed a set of Finite Element Method (FEM) simulations of a polymeric matrix volume (a cube of $200 \times 200 \times 200$ nm^3) containing an increasing number of randomly dispersed spherical magnetite NPs (10 nm mean radius, from 0.1312 to 0.3730% volume ratio), using the commercial code Comsol Multiphysics^{TM}. An example of the simulation control volume is given in Fig. 9 (top), where the tetrahedral mesh of Lagrangian cubic elements is shown, referring to a distribution of 50 NPs. The simulation parameters are given in Table 2 along with their sources; we applied the following stability boundary conditions: matrix and NPs free to deform, control volume center fixed; initial compressive stress corresponding to a volume contraction of 10% to simulate polymerization; thermal load from a reference temperature of 273.15 K down to 1 K. Depending on the NP volume ratio, the complexity of the system ranges between 11 and 19 K elements, with a number of degrees of freedom ranging from 100 to 150 K and a solution time (Intel® Core^{TM} 2 Quad Q9550 2.83 GHz, 4 GB DDR3) ranging from 110 to 280 s. The stress evaluation was done integrating over each NP the Von Mises stress (σ_{NP}^{VM}), which represents the deviatoric, non-hydrostatic component of the compressive/tensile state of a material (Sadd 2009). According to our simulation, the stress tensor exhibits large negative local components indicating predominant compression effects on NPs; the average von Mises stress—which is by definition a positive quantity—is very large, pointing to a highly anisotropic compression. The results for $<\sigma_{NP}^{VM}>$ are given in Fig. 9 (bottom left), as functions of the composite temperature and the NP volume ratio, together with a linear fit to the computed values. We can see that: (a) $<\sigma_{NP}^{VM}>$ increases with decreasing T owing to the difference between thermal expansion parameters of matrix and dispersoid (see Table 2), and the temperature behavior is pretty linear; (b) above 0.25 wt% the compressive stress at a fixed temperature starts to increase; (c) the thermal load rate increases with dispersoid volume fraction also (bottom right). Remarkably, in our model system the non-hydrostatic compressive stress component would exceed 400 MPa above 0.25 wt% at room temperature.

This simulation provides support to the hypothesis that $|K_{eff}|$ of magnetite NPs dispersed in PEGDA can be significantly affected by stress anisotropy. Of course, the compressive stress existing in our samples is expected to be much lower than this estimate. In fact, the simulation is based upon simplifying assumptions, such as a fully homogeneous polymeric matrix. The presence of inhomogeneities in the real polymeric matrix provides an important channel for the relaxation of the local stress and for its significant reduction with respect to the ideal case.

Concluding remarks

Magnetite NPs with a diameter of about 8 nm obtained by a chemical route display overall magnetic properties best described by the ISP model,

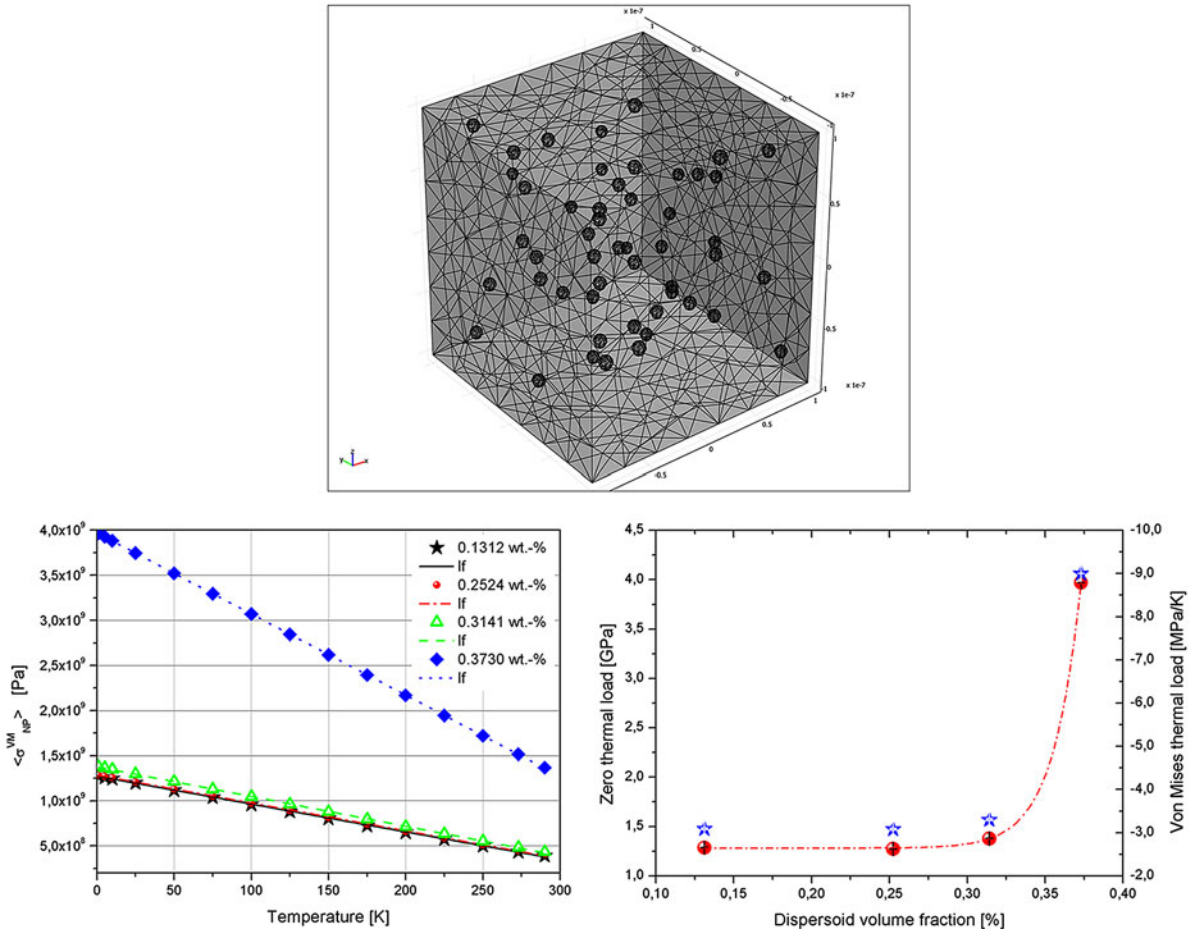

Fig. 9 *Top* representation of the FEM simulation mesh elements, showing the randomly distributed spherical magnetite NPs (0.3141 wt%); *bottom left* integration of the Von Mises stress over the NPs for different temperatures and volume ratios in the composite; *bottom right* temperature dependence of the zero K Von Mises stress (*left*, *circles*) and of the Von Mises thermal load (*right*, *stars*). The exponential fit to the zero K stress is a guide for the reader

Table 2 Physical parameters of polymeric matrix and dispersoid used in FEM simulations

Physical parameters	Matrix	Dispersoid
Density [kg m^{-3}]	1190	5150
Thermal expansion [K^{-1}]	7×10^{-4} [a]	1.2×10^{-4} [b]
Poisson modulus [-]	0.40	0.37[c]
Shear modulus [GPa]	Isotropic	100
Young modulus [GPa]	3	120[d]
Thermal conductivity [Wm^{-1} K^{-1}]	0.19	400
Thermal capacity [J kg^{-1} K^{-1}]	1420	385

[a] Taken from literature (Lin and FreemanBD 2006)

[b] Taken from literature (Nikolaev and Shipilin 2000)

[c] Taken from literature (Chicot et al. 2010)

[d] Taken from literature (Kester et al. 1999)

indicating the presence of non-negligible long-range magnetic interactions. Low-temperature hysteretic properties of as-prepared NPs are in good agreement with the prediction of the Stoner-Wohlfarth model for cubic-symmetry magnetic anisotropy, indicating that the magneto-crystalline term dominates over shape anisotropy. The presence of a significant surface anisotropy is ruled out in these NPs by considering that the value of the coercive field is fully compatible with a K_1 value typical of bulk magnetite.

Dispersion of magnetite NPs in PEGDA polymeric matrix does not modify the ISP behavior but has important consequences on the low-temperature hysteretic properties. In particular, the coercive field is strongly reduced with increasing NP concentration in

PEGDA, a result explained by invoking the presence of strong compressive stresses on NPs induced by the polymeric matrix and introducing a stress-anisotropy term which acts to counterbalance the magneto-crystalline anisotropy. The hypothesis is substantiated by a numeric simulation.

In conclusion, both single-particle effects (responsible for the measured hysteretic properties) and collective effects (approximately accounted for by a mean-field approach such as the ISP model) play a role in the examined systems, the former dominating magnetic properties at low temperatures.

Acknowledgments The Authors thank Dr. Luciano Pilloni, Dr. Patrizia Imperatori, and Dr. Lorenzo Vescovo for SEM observations, XRD measurements, and for helping in producing the polymeric samples, respectively. This study has been partially supported by the industrial Research Project PrinTag of Regione Piemonte.

References

Allia P, Coisson M, Knobel M, Tiberto P, Vinai F (1999) Magnetic hysteresis based on dipolar interactions in granular magnetic systems. Phys Rev B 60:12207–12218. doi:10.1103/PhysRevB.60.12207

Allia P, Coisson M, Tiberto P, Vinai F, Knobel M, Novak MA, Nunes WC (2001) Granular Cu-Co alloys as interacting superparamagnets. Phys Rev B 64: 144420-1–144420-12. doi:10.1103/PhysRevB.64.144420

Bickford LR, Pappis J, Stull JR (1955) Magnetostriction and permeability of magnetite and cobalt-substituted magnetite. Phys Rev 99:1210–1214

Chicot D, Roudet F, Zaoui A, Louis G, Lepingle V (2010) Influence of visco-elasto-plastic properties of magnetite on the elastic modulus: multicyclic indentation and theoretical studies. Mater Chem Phys 119:75–81. doi:10.1016/j.matchemphys.2009.07.033

Chiolerio A, Vescovo L, Sangermano M (2010) Conductive UV-cured acrylic inks for resistor fabrication: models for their electrical properties. Macromol Chem Phys 211: 2008–2016. doi:10.1002/macp.201090043

Cullity BD (1972) Introduction to magnetic materials. Addison-Wesley, Reading

Dai Q, Berman D, Virwani K, Frommer J, Jubert PO, Lam M, Topuria T, Imaino W, Alshakim N (2010) Self-assembled ferrimagnet-polymer composites for magnetic recording media. Nano Lett 10:3216–3221. doi:10.1021/nl1022749

Gangopadhyay R, De A (2000) Conducting polymer nanocomposites: a brief overview. Chem Mater 12:608–622. doi:10.1021/cm990537f

Garcia-Otero J, Garcia-Bastida AJ, Rivas J (1998) Influence of temperature on the coercive field of non-interacting fine magnetic particles. J Magn Magn Mater 189:377–383. doi:10.1016/S0304-8853(98)00243-1

Gittleman JI, Abeles B, Bozowski S (1974) Superparamagnetism and relaxation effects in granular Ni–SiO_2 and Ni–Al_2O_3 films. Phys Rev B 9:3891–3897

Guardia P, Batlle-Brugal B, Roca AG, Iglesias O, Morales MP, Serna CJ, Labarta A, Batlle X (2007) Surfactant effects in monodisperse magnetite nanoparticles of controlled size. J Magn Magn Mater 316:e756–e759. doi:10.1016/j.jmmm.2007.03.085

Jalali M, Wuthrich R (2009) Improving electromagnetic shielding of composite structures with metallic nanoparticles synthesized by electrochemical discharges. Proceedings of international symposium on electromagnetic compatibility. doi:10.1109/EMCEUROPE.2009.5189689

Jaworek A, Sobczyk AT (2008) Electrospraying route to nanotechnology: an overview. J Electr 66:197–219. doi:10.1016/j.elstat.2007.10.001

Kester E, Rabe U, Presmanes L, Tailhades Ph, Arnold W (1999) Measurement of mechanical properties of nano-scaled ferrites using atomic force microscopy at ultrasonic frequencies. Nanostruct Mater 12:779–782. doi:#10.1016/S0965-9773(99)00235-4

Kumagai M, Kano MR, Morishita Y, Ota M, Imai Y, Nishiyama N, Sekino M, Ueno S, Miyazono K, Kazunori K (2009) Enhanced magnetic resonance imaging of experimental pancreatic tumor in vivo by block copolymer-coated magnetite nanoparticles with TGF-β inhibitor. J Contr Release 140:306–311. doi:10.1016/j.jconrel.2009.06.002

Lee WK, Dai Z, King WP, Sheehan PE (2010) Maskless nanoscale writing of nanoparticle—polymer composites and nanoparticle assemblies using thermal nanoprobes. Nano Lett 10:129–133. doi:10.1021/nl9030456

Li S, Lin MM, Toprak MS, Kim DK, Muhammed M (2010) Nanocomposites of polymer and inorganic nanoparticles for optical and magnetic applications. Nano Rev 1: 5214-1–5214-19. doi:10.3402/nano.v1i0.5214

Lin H, Freeman BD (2006) Gas permeation and diffusion in cross-linked poly(ethylene glycol diacrylate). Macromolecules 39:3568–3580. doi:10.1021/ma051686o

Nicolais L, Carotenuto G (2005) Metal-polymer nanocomposites. John Wiley & Sons, Inc, Hoboken. doi:10.1002/0471695432

Nikolaev VI, Shipilin AM (2000) On the thermal expansion of nanoparticles. Phys Solid State 42–1:112–113. doi:10.1134/1.1131176

Pankhurst QA, Connolly J, Jones SK, Dobson J (2003) Applications of magnetic nanoparticles in biomedicine. J Phys D Appl Phys 36:R167–R181. doi:10.1088/0022-3727/42/22/224001

Sadd MH (2009) Elasticity: theory, applications and numerics. Academic Press, Burlington

Shull RD, Kerch HM, Ritter JJ (1994) Magnetic properties of colloidal silica: potassium silicate gel/iron nanocomposites. J Appl Phys 75:6840–6842. doi:10.1063/1.356802

Sohn BH, Cohen RE, Papaefthymiou GC (1998) Magnetic properties of iron oxide nanoclusters within microdomains of block copolymers. J Magn Magn Mater 182:216–224

Sun S, Zeng H, Robinson DB, Raoux S, Rice PM, Wang SX, Li G (2004) Monodisperse MFe_2O_4 (M: Fe, Co, Mn) nanoparticles. J Am Chem Soc 124:8204–8205. doi:10.1021/ja0380852

Tartaj P, Gonzalez-Carreno T, Serna CJ (2001) Single-step nanoengineering of silica coated maghemite hollow spheres with tunable magnetic properties. Adv Mater 13:1620–1624. doi:10.1002/1521-4095(200111)

Vázquez M, Luna C, Morales MP, Sanz R, Serna CJ, Mijangos C (2004) Magnetic nanoparticles: synthesis, ordering and properties. Phys B 354:71–79. doi:10.1016/j.physb.2004.09.027